Characterization of dendritic growth in Fe–C system using time-resolved X-ray tomography and physics-based filtering

IOP Conf. Series: Materials Science and Engineering **529** (2019) 012023 doi:10.1088/1757-899X/529/1/012023

Characterization of dendritic growth in Fe–C system using time-resolved X-ray tomography and physics-based filtering

H Yasuda, T Kawarasaki, Y Tomiyori, Y Kato and K Morishita*

Department of Materials Science and Engineering, Kyoto University, Sakyo, Kyoto, 606-8501, Japan
* Present address: Department of Materials Science and Engineering, Kyushu University, Nishi-ku, Fukuoka 819-0395, Japan

E-mail: yasuda.hideyuki.6s@kyoto-u.ac.jp

Abstract. Time-resolved *in situ* tomography of dendritic growth in Fe–0.45 mass% C carbon steel was performed using synchrotron radiation X-rays at SPring-8 synchrotron radiation facility (Japan) with improvement of the image quality using a physics-based filter. The voxel size of the reconstructed image was approximately 6.5 μm × 6.5 μm × 6.5 μm, and the time resolution (duration of 360° rotation) was 4 s (0.25 rps). Three-dimensional images of the dendrites were reconstructed even without image processing; however, the low contrast resolution in Fe–C alloys led to poor image quality. Consequently, it was impossible to precisely track the solid/liquid interface or evaluate the average curvature. To improve the image quality, a physics-based filter (a PF filter) was developed using a phase-field model. In the PF filter, images were retrieved in terms of interface curvature. The PF filter significantly improved the computed tomography image quality. As a result, dendritic growth was clearly observed even in Fe–C alloys. Moreover, the average curvature of the solid/liquid interface was evaluated as a function of solidification time (solid fraction). The ability to systematically characterize growing dendrites will be beneficial for modeling and simulation of solidification phenomena.

1. Introduction

Time-resolved *in situ* observations using synchrotron radiation X-rays with high brilliance and high coherency have allowed us to observe solidification and related phenomena such as the solidification of low-melting-temperature alloys (Sn, Zn, and Al alloys) [1-5] and high-melting-temperature alloys (cast iron, carbon steel, and stainless steel) [6-11]. These direct observations are beneficial for understanding microstructural evolution and casting defect formation as well as for constructing physical models, enabling, for example, the direct observation of the massive transformation in Fe–C alloys [9]. The γ phase (austenite, face-centered cubic) has long been considered to be produced via a peritectic reaction between the δ phase (ferrite, body-centered cubic) and liquid phase during solidification of carbon steel with a carbon content of less than 0.5 mass%. However, time-resolved *in situ* observations of Fe–C alloys [9, 10, 12] revealed that a massive transformation, in which the δ phase transforms into the γ phase in the solid state, is dominantly selected. In addition to radiography, laser-scanning confocal microscopy has also revealed this massive transformation of the δ phase into the γ phase [13]. This massive transformation was also observed in Fe–Cr–Ni alloys [14].

All these observations of solidification and massive transformation in Fe-based alloys were performed using X-ray transmission imaging of a thin specimen (typically 100 μm), which has some

inherent limitations. Solute diffusion and the development of dendrite arms are constrained in thin specimens. The limited space also affects the curvature of the solid/liquid interface and dendrite arm spacings. Time-resolved computed tomography (referred to as 4D-CT), which allows *in situ* observation of the microstructural evolution, can be applied to overcome these issues for characterization of the 3D solidification structure.

A critical issue for the 3D observation of dendrites during solidification is the time resolution. Ultrafast 4D-CT was performed using synchrotron radiation X-rays at the European Synchrotron Radiation Facility (ESRF) to observe the microstructural evolution in Al–4 mass% Cu alloys (1 mm in diameter, cooling rate of 0.1 K/s) [15]. A pink beam (peak energy of 40 keV) was used to increase the transmission X-ray intensity. For the reconstruction, 500 projections over 180° rotation (10 s/rotation) were used. The 4D-CT observations revealed the formation of solid grains isolated by a liquid phase, a change in the solid fraction during cooling, shrinkage due to solidification, and the solid/liquid interfacial area (f_s>0.7). In addition, 4D-CT was used to observe the melting and solidification of a metal-matrix nanocomposite in Al–Mg–Si alloys (AI-6082) with the addition of 0.54 vol.% Y_2O_3 particles (~500 nm) [16]. In total, 1440 projections over 180° (8.6 s/rotation) were obtained using a pink beam (peak energy of 17.6 keV). Coarsening of the dendrite arms in Al–15 mass% Cu alloys was also observed using 4D-CT (monochromatized X-ray: 30 keV, 721 projections over 180°, voxel edge length: 1.4 μm), and the results were compared with phase-field simulations [17]. More recently, the dendrite morphology during the early stage of solidification in Al–24 mass% Cu alloys (1 mm in diameter) was also observed using 4D-CT by applying interlaced view sampling (interval between reconstruction: 1.8 s, voxel edge length: 0.65 μm) [18]. The morphologies of the primary and secondary dendrite arms were well reconstructed using the time-interlaced model-based iterative reconstruction (TIMBIR) method [18]. Semi-solid deformation in Al–15 mass% Cu alloys was also observed using 4D-CT (3 mm in diameter, 720 projections over 180°, interval between reconstruction: 4 s) [19]. The study revealed that transgranular liquation cracking of grains isolated by the remaining liquid phase could occur even at low stress (1–40 MPa) [19].

In addition, 4D-CT has been applied to observe the solidification in Ni–14 mass% Hf, Fe–11 mass% Hf, and Co–18 mass% Hf alloys (1.8 mm in diameter) at high temperatures [20]. Higher contrast resolution between the solid and liquid phases in the alloys containing Hf (an absorption edge of 65.351 keV) was achieved using high-energy X-rays (65–80 keV). The 4D-CT technique clearly revealed the solid/liquid interface even in Ni, Fe, and Co alloys.

To the best of our knowledge, however, observation of the evolution of the 3D structure in alloys with low contrast resolution such as Fe–C steels (Fe–C–Mn–Si alloys) remains challenging. For carbon steels (Fe–C–Mn–Si alloys), X-rays with relatively high energy are required because of the large X-ray absorption coefficient of iron; however, X-rays with lower energy are preferable to increase the contrast resolution. Our previous study [21] showed that 3D images of dendrites, even in Fe–C alloys, could be obtained using 4D-CT. This study demonstrates the use of 4D-CT combined with image processing using a phase-field model, with the curvature of the solid/liquid interface evaluated from the processed images.

2. Experiments

Time-resolved tomography experiments were performed at beamline BL20XU of SPring-8 (synchrotron radiation facility, Hyogo, Japan) [21]. The X-rays were monochromatized using a Si (111) double-crystal monochromator. An X-ray energy of 37.7 keV was selected. Figure 1 shows the 4D-CT apparatus and configuration of the rod specimen (0.8 mm in diameter), X-ray beam (approximately 3 mm in width and 3 mm in height), and beam monitor (pixel size 6.5 μm × 6.5 μm). The specimen was rotated at 0.25 rps (4 s/rotation), and transmission images were obtained at 100 fps. Namely, convolution back-projection (CBP) image reconstruction was performed using 200 transmission images (approximately 200 × 200 pixels) over 180° rotation. It should be noted that 200 projections were not sufficient to reconstruct a cross-section (specimen area of 200 × 200 pixels) using normal procedures.

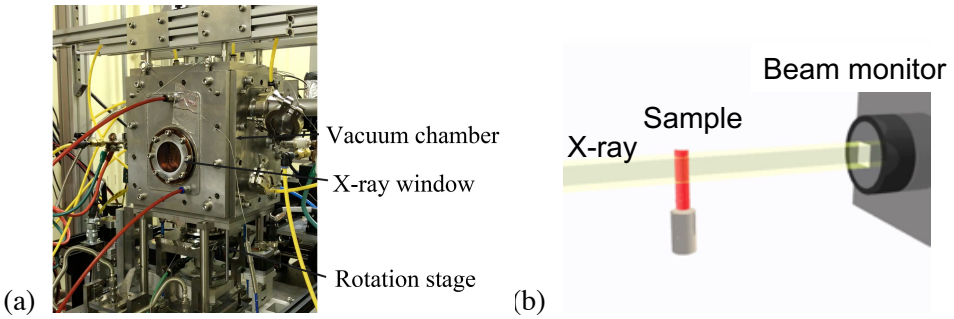

Figure 1. (a) Time-resolved tomography apparatus and (b) configuration of X-ray beam, specimen, and beam monitor.

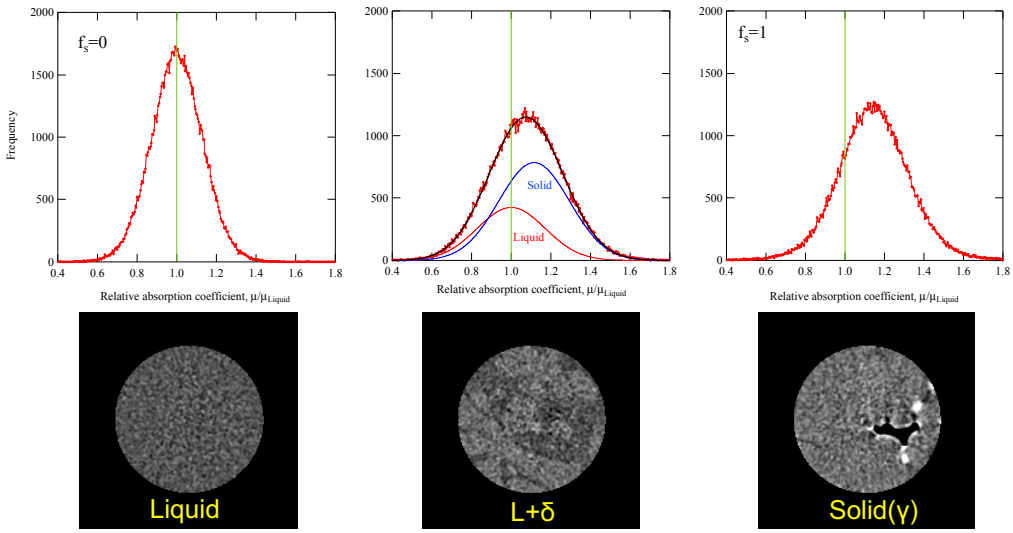

Figure 2. Reconstructed images (bottom) and distribution of the relative absorption coefficient (top). The relative absorption coefficient was normalized by that of the liquid phase before solidification.

Conventional carbon steel, Fe–0.45C–0.6Mn–2Si (mass%), was used as the specimen. The specimen rod was inserted into a sintered Al_2O_3 pipe (inner and outer diameters of 0.8 and 2 mm, respectively). The specimen was melted and then cooled at a cooling rate of 0.17 K/s in a vacuum atmosphere (approximately 1 Pa). The temperature gradient at the specimen was less than 1 K/mm. Projected images were continuously recorded during the cooling procedure.

3. Results and Discussion

3.1. Solid fraction

Figure 2 presents the reconstructed images without image processing and plots of the distribution of the relative absorption coefficient. The relative absorption coefficient was obtained by normalizing the absorption coefficient to that of the liquid phase. Thus, the average value in the distribution at $f_s = 0$ (liquid phase) was 0, as shown in Fig. 2(a). The full width at half maximum was as large as 40% because of the low signal-to-noise (S/N) ratio, which arose from the low contrast resolution and the small number of projected images (200 projection images). Although dendrite arms were visible in the reconstructed images, as shown in Fig. 2(b), it was impossible to smoothly track the solid/liquid interface.

As observed in Fig. 2(c), the average value of the absorption coefficient was 1.08 at $f_s = 1$ (austenite phase). Thus, the change in the absorption coefficient during solidification was measured even though the S/N ratio was low. The distribution of the absorption coefficient was well fitted by two Gaussian curves for the liquid and solid phases, as shown in Fig. 2(b). Figure 3 shows the solid fraction, f_s, obtained by the fitting. The solid fraction roughly followed a square-root law and rapidly increased at 740 s owing to the transformation from the δ to γ phase. Because the transformation occurred below the peritectic temperature, solidification was immediately completed after the transformation.

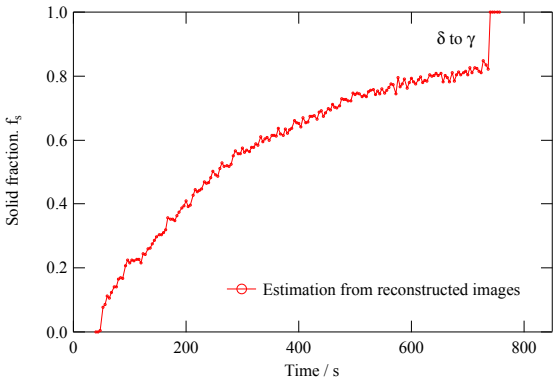

Figure 3. Solid fraction estimated from the distribution of the relative absorption coefficient.

The present results indicate that a 3D solidification structure can be obtained using 4D-CT. However, considerable noise was introduced because of the low contrast resolution of Fe–C alloys in the reconstructed images. The change in the solid fraction during solidification was evaluated despite the considerable noise.

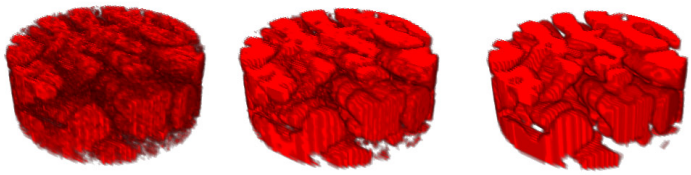

Figure 4. Reconstructed images: (a) raw data and date after (b) Gaussian filtering and (c) PF filtering.

3.2. Filtering using a phase-field model

The considerable noise introduced during the reconstruction process by the low contrast resolution needed to be removed to track the solid/liquid interface and evaluate the interfacial area and curvature. In conventional image processing, the reconstructed images are improved by blurring/smoothing, which reduces detail, and unsharp masking, which increases acutance. These image procedures are widely used for various applications. As shown in Fig. 4, the smoothing (Gaussian filter) improved the reconstructed image, and consequently, dendritic arms were clearly observed in the 3D reconstructed image. Thus, conventional image processing was sufficient to observe dendrites. Although the surface became smooth,

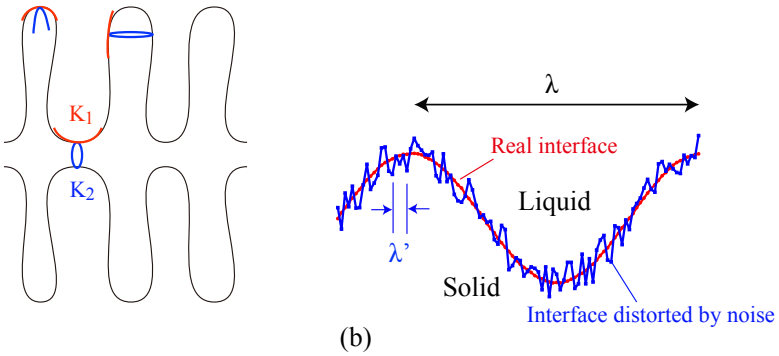

Figure 5. (a) Schematic illustration of dendrite arms and (b) solid/liquid interface distorted by noise.

the noise (on the order of the voxel size) still remained and degraded the evaluation of the curvature. Furthermore, the filtering conditions are often determined by sensory experience.

We attempted to develop an image processing procedure that overcomes these disadvantages. Figure 5(a) presents a schematic illustration of the dendrite shape. The average curvature, K, is defined by

$$\frac{1}{\mathrm{K}} = \frac{1}{\mathrm{K}_1} + \frac{1}{\mathrm{K}_2}. \tag{1}$$

Here, K_1 and K_2 are defined as shown in Fig. 5(a). If a pure substance is placed under isothermal conditions, the average curvature should be equal at any solid/liquid interface point in equilibrium. For alloy dendrites under isothermal conditions, the presence of a non-uniform distribution of solutes modifies the average curvature. However, the distributions of solute concentrations will be rather small between the dendrite arms (the typical scale ranges from 10 to 100 μm).

Figure 5(b) shows the solid/liquid interface distorted by noise induced during the reconstruction process. The typical period of the noise induced in the reconstruction procedure is on the order of the voxel size (λ'). When the typical period (λ) of the dendrite arms is larger than that of the noise, as shown in Fig. 5(b), the real interface can be tracked by removing the short-wavelength component in the reconstructed 3D images. As the average curvature is significantly distorted by the short-wavelength component, we developed an image processing procedure based on the average curvature as one possible approach.

Phase-field models were developed to simulate microstructural evolution such as dendritic growth [22-25]. These phase-field models have certain advantages. For instance, the model does not explicitly consider the solid/liquid interface, and 3D images are easily converted into a phase field. In addition, the model naturally includes the physical principles that control the microstructural evolution, such as the curvature effect. In this study, a phase-field model was used for filtering the reconstructed images (referred to as PF filtering). In the first step, 3D images, such as those in Fig. 2, were converted into a phase field using eq. (1). In the present case, each CT voxel was divided into eight phase-field voxels (2 × 2 × 2 voxels).

$$\phi = \begin{cases} 0 & \left(\bar{\mu} < \mu_L\right) \\ \dfrac{\bar{\mu} - \mu_L}{\mu_S - \mu_L} & \left(\mu_L \le \bar{\mu} \le \mu_S\right) \\ 1 & \left(\bar{\mu} > \mu_S\right) \end{cases} \tag{2}$$

In the second step, the phase field was sequentially calculated using eqs. (2)–(4).

$$\Delta\phi = -\left(M\Delta t\right)\left[6\phi\left(1-\phi\right)\Delta f + 2\phi\left(1-\phi\right)\left(1-2\phi\right)W - \varepsilon^2\nabla^2\phi\right] \tag{3}$$

$$\Delta f = -\sigma K = -\sigma\frac{2}{r} \tag{4}$$

$$W = \frac{3\sqrt{2}\sigma}{\delta} \tag{5}$$

$$\varepsilon^2 = 3\sqrt{2}\sigma\delta \tag{6}$$

Here, ϕ is the phase field, t is the time, M is the interface mobility, Δf is the driving force of solidification expressed by eq. (3), σ is the solid/liquid interfacial energy (0.2 J/m^2), and δ is the thickness of the solid/liquid interface. The thickness δ used in this study was 2–4 times larger than the edge length of the phase-field voxel. W and ε^2 were determined from the solid/liquid interfacial energy and thickness of the solid/liquid interface. In the PF filter, the value of $M\Delta t$ was selected such that the change in ϕ was less than 0.01 at each step.

Equation (4) expresses the driving force for the interface motion. In the third step, an appropriate value for r in eq. (4) is determined. Once the parameters are given, the PF filtering evolves the

solid/liquid interface and the solid fraction converges to a certain value. In this study, the parameter *r* was selected such that the solid fraction estimated from the phase field was equal to that estimated from the distribution of the relative absorption coefficient, as shown in Fig. 2(b). In other words, the solid fraction estimated from 4D-CT was used as a restraint condition in the PF filtering. Figure 2(c) shows an example of the reconstructed dendrites after the PF filtering. Although there is no significant difference between Figs. 4(b) and (c), the solid/liquid interface was modified by the PF filtering. The details are provided in the next section.

3.3. Characterization of dendrite shape

Figure 6 presents the cross-sectional images and the distributions of the average curvature. The numbers in the figure represent the number of iterations of the PF filtering. As the number of iterations increased, the noise was remarkably reduced; the shapes of the dendrite arms were clearly identifiable in the cross-sectional images after 1000 and 1500 steps. It was thus possible to track the solid/liquid interface in the cross-sectional images after 1000 and 1500 steps.

As shown in the histogram of the average curvature in Fig. 6, the distribution of the average curvature was remarkably modified by the PF filter. In the reconstructed images without the PF filtering (0 steps), an intense artifact induced by noise in the rectangular coordinate system produced 5–6 sharp peaks. The average curvature of 10^{6} m (curvature radius: 2 μm) is much larger than the real curvature, indicating that the noise contributed to the large curvatures. After the PF filter was applied, the distribution became Gaussian-like and the full width at half maximum gradually decreased with increasing number of iterations. In principle, as expressed by eq. (2), the PF filtering eliminated distortion with short wavelength. Thus, the PF filter was effective in reducing noise induced during the reconstruction process.

Figure 7 presents 3D images of the growing dendrites and a plot of the average curvature as a function of solidification time (the solid fraction was also determined from Fig. 2). Even the secondary dendrite

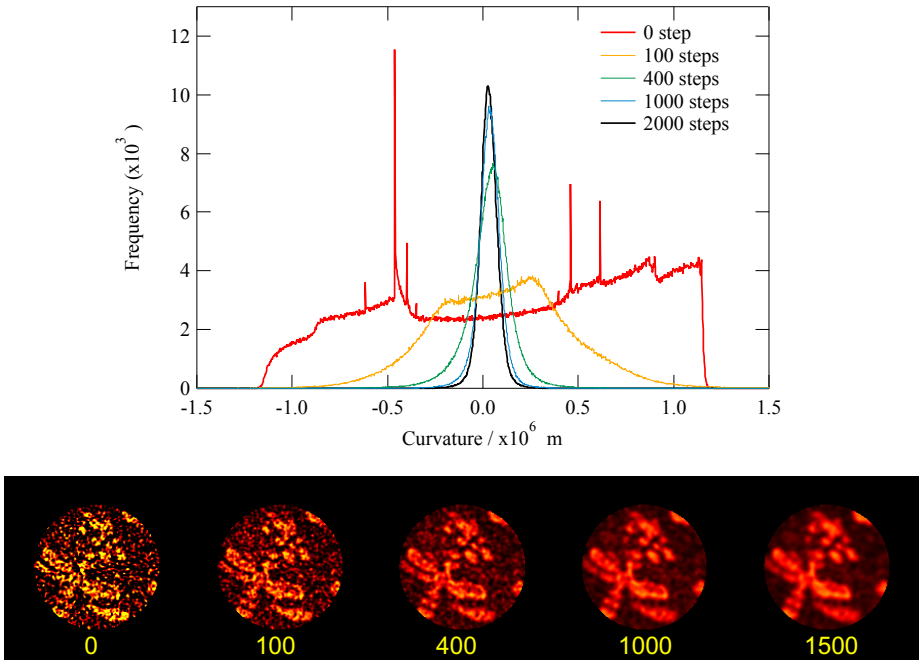

Figure 6. Filtered images (bottom) and distribution of solid/liquid interface curvature (top) as a function of number of iterations.

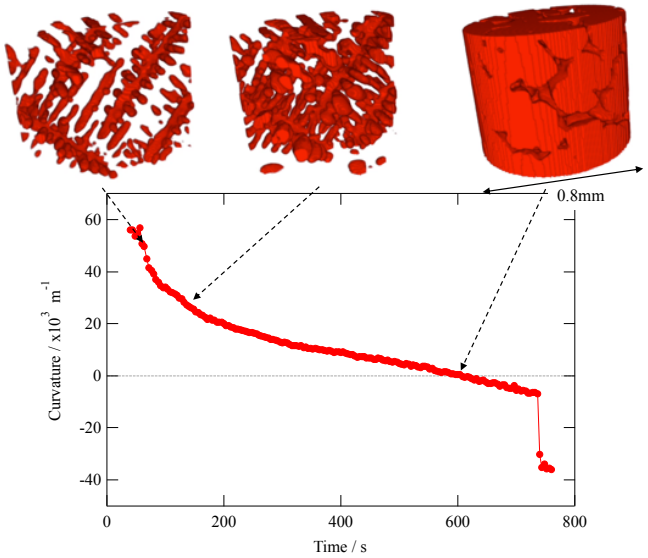

Figure 7. 3D images of dendrites after filtering (top) and plot of average curvature as a function of solidification time (bottom).

arms were clearly identified in each time step because of the elimination of noise. In addition, the average curvature of the solid/liquid interface as a function of solidification time (solid fraction) was successfully evaluated, as shown in the top images in Fig. 7. The average curvature rapidly decreased at the beginning of solidification, and then, the decreasing rate was gradually reduced. The average curvature became negative at a solid fraction of 0.75. The rapid decrease at 750 s was caused by the massive transformation from the δ to γ phase [9]. It should be noted that the filtered 3D images were uniquely obtained by the PF filtering in which the solid fraction determined by 4D-CT was used as a constraint parameter. The constraint condition enabled systematic reproduction of the dendrite shape. Further studies are needed to evaluate the accuracy of this process and to discuss its limitations.

These results demonstrate that 4D-CT with a PF filter can be used for time-resolved *in situ* 3D observation of dendritic growth and quantitative characterization of growing dendrites (i.e., the curvature, interfacial area, and secondary arm spacing) even in Fe–C alloys. This improved understanding of dendrite shapes will be beneficial for modeling and simulation of solidification phenomena. Moreover, 4D-CT with PF filtering enables unique characterization of growing dendrites. The validity of the use of the PF filter should be examined in a future study.

4. Summary

Time-resolved *in situ* tomography was used to observe the dendritic growth and to characterize growing dendrites in Fe–0.45C–0.6Mn–2Si (mass%) alloys.

- In this work, 4D-CT was performed using monochromatized X-rays with an energy of 37.7 keV. The specimen was rotated at 0.25 rps, and 200 projections over 180° rotation were used for the reconstruction.
- Dendrite arms were recognized in the reconstructed images without the filter (pixel edge length: 6.5 μm). However, it was impossible to track the solid/liquid interface or evaluate the average curvature of the solid/liquid interface because of the poor image quality.
- A PF filtering procedure was developed to improve the quality of the reconstructed images. For the PF filtering, the solid fraction determined from the 4D-CT was used as a constraint condition. The driving force of solidification in the PF filtering was a key parameter for the filtering. Use

of this PF filter with an appropriate value of this driving force significantly improved the image quality.

- The primary and secondary dendrite arms were clearly identified at each time step. Time evolution of three-dimensional dendrites was well reproduced from the filtered images.
- The distribution of the average curvature was Gaussian-like with a relatively low full width at half maximum. In addition, the average curvature was determined as a function of solidification time (solid fraction).
- 4D-CT with the PF filtering is expected to improve the characterization of growing dendrites even in alloys with relatively low contrast resolution. The resulting quantitative data can be used for modeling and simulation of solidification phenomena.

Acknowledgments
The synchrotron radiation experiments were performed as general projects at beamlines BL20B2 and BL20XU at SPring-8 (JASRI), Japan. The study was developed by "Heterogeneous Structure Control: Towards Innovative Development of Metallic Structural Materials" in Industry–Academia Collaborative R & D Program (JST). An observation technique including the PF filter was developed by a Grant-in-Aid for Scientific Research (S) (No. 17H06155). We thank Tiffany Jain, M.S., from Edanz Group (www.edanzediting.com/ac) for editing a draft of this manuscript.

References

[1] Mathiesen R H, Arnberg K, Mo F, Weitkamp T, Snigirev A 1999 *Phys. Rev. Lett.* **83** 5062
[2] Yasuda H, Ohnaka I, Kawasaki K, Sugiyama A, Ohmichi T, Iwane J, Umetani K 2004 *J. Cryst. Growth* **262** 645
[3] Mangelinck-Noel N, Nguyen-Thi H, Reinhart G, Schenk T, Cristiglio V, Dupouy M D, Gastaldi J, Billia B, Hartwig J 2005 *J. Phys. D,* **38** A28
[4] Li B, Brody H D, Black D R, Burdette H E, Rau C 2006 *J. Phys. D* **39** 4450
[5] Wang T M, Xu J J, Xiao T Q, Xie H L , Li J, Li T J, Cao Z Q 2010 *Phys. Rev. E* **81** 042601
[6] Yasuda H, Yamamoto Y, Nakatsuka N, Nagira T, Yoshiya M, Sugiyama A, Ohnaka I, Umetani K, Uesugi K 2008 *Int. J. Cast Met. Res.* **22** 15
[7] Yasuda H, Nagira T, Yoshiya M,, N. Nakatsuka, A. Sugiyama, K. Uesugi, K. Umetani, ISIJ Int. 51 (2011) 402.
[8] Nagira T, Gourlay C M, Sugiyama A, Uesugi M, Kanazawa M, Yoshiya M, Uesugi K, Umetani K, Yasuda H 2011 *Scripta Mater.*, **64** 1129
[9] Yasuda H, Nagira T, Yoshiya M, Sugiyama A, Nakatsuka N, Kiire M, Uesugi M, Uesugi K, Umetani K, Kajiwara K 2012 *IOP Conf. Ser.: Mater. Sci. Eng.* **33** 012036
[10] Nishimura T, Morishita K, Nagira T, Yoshiya M, Yasuda H 2015 *IOP Conf. Ser.: Mater. Sci. Eng.* **84** 012062
[11] Yamane K, Yasuda H, Sugiyama A, Nagira T, Yoshiya M, Morishita K, Uesugi K, Takeuchi A, Suzuki Y 2015 *Metall. Mater. Trans, A* **46A** 4937
[12] Nishimura T, Morishita K, Yoshiya M, Nagira T, Yasuda H **2019** *Tetsu-to-Hagané* **105** in press.
[13] Griesser S, Reid M, Bernhard C, Dippenaar R 2014 Acta Mater. **67** 335
[14] Nishimura T, Matsubayashi R, Morishita K, Yoshiya M, Nagira T, Yasuda H 2019 *ISIJ International* **59** in press.
[15] Ludwig O, Dimichiel M, Salvo L, Suery M, Falus P 2005 *Metall Mat Trans A* **36A** 1515
[16] Daudin R, Terzi S, Lhuissier P, Salvo L, Boller E 2015 *Mater. Design* **87** 313
[17] Aagesen L K, Fife J L, Lauridsen E M, Voorhees P W 2011 *Scripta Mater.* **64** 394
[18] Gibbs J W, Mohan K A, Gulsoy E B, Shahani A J, Xiao X, Bouman C A, De Graef M, Voorhees P W 2015 *Scientific Reports* **5** 11824
[19] Cai B, Karagadde S, Yuan L, Marrow T J, Connolley T, Lee P D 2014 *Acta Mater.* **76** 371
[20] Cai B, Wang J, Kao A, Pericleous K, Phillion A B, Atwood R C, Lee P D 2016 *Acta Mater.* **117** 160

[21] Yasuda H, Tomiyori Y, Kawarazaki T, Kato K, Morishita K 2018 *Proc. Solidification and Gravity VII* 75
[22] Kobayashi R 1993 *Physica D* **63** 410
[23] Wheeler A A, Murray B T, Schaefer R 1993 *Physica D* **66** 243
[24] Wang S-L, Sekerka R F. 1996 Phys. Rev. E **53** 3760
[25] Karma A, Rappel W-J 1996 *Phys. Rev. E* **53** R3017